A NOVEL PERCEPTUALLY-ORIENTED APPROACH FOR SKIN TUMOR SEGMENTATION

QAISAR ABBAS[1], M. EMRE CELEBI[2] AND IRENE FONDÓN GARCÍA[3]

[1]Department of Computer Science
National Textile University
Sheikhupura Road, Faisalabad 37610, Pakistan
drqaisar@ntu.edu.pk; qaisarabbasphd@gmail.com

[2]Department of Computer Science
Louisiana State University
Shreveport, LA, USA
ecelebi@lsus.edu

[3]Escuela Superior de Ingenieros
Universidad de Sevilla
Camino de los Descubrimientos, s/n, 41092 Sevilla, Spain
irenef@us.es

ABSTRACT. *In this paper, a novel and automatic approach for skin tumor segmentation is presented. Tumors images with a dermoscope are usually affected by hairs, low contrast, specular reflections, shadows due to uneven illumination, etc, making the segmentation step extremely difficult. The proposed technique, mainly based on region-based active contour algorithm extended to multiple region detection, is performed in the CIECAM02 based uniform color space to achieve an adaptation to human perception. It also avoids the limitations introduced by the conventional active contour algorithms: level set initialization step, fixed regularization parameters, and overlapping of the contours in the presence of multiple objects. The improved region-based active contour technique automatically initializes the level set curves by a blob technique, determines the required parameters for convergence and utilizes a conditional function to avoid overlapping contours. In this new algorithm, dermoscopic images are preprocessed in order to correct specular reflection, improve contrast and remove hairs with techniques based on homomorphic filtering, optimal contrast adjustment and exemplar-based inpainting, respectively. To validate the segmentation results obtained, comparisons with three state-of-the-art segmentation algorithms have been performed. Experimental results on 170 images gave an average segmentation error of 4.10 ± 2.42. In terms of visual perception, the integration of a uniform color space makes the algorithm closer to experts than the other state-of-the-art methods. The preprocessing steps included and the improved segmentation algorithm make the technique useful in practical applications.*
Keywords: Skin tumor segmentation, Image enhancement, CIECAM02 color appearance model, Visual perception, Region-based active contour model

1. **Introduction.** Malignant melanoma (*MM*) [1] is one of the rare skin cancers with an increasing incidence rate. In the United States alone, the number of new cases and deaths associated with *MM* in 2010 is estimated to be 68,130 and 8,700, respectively [2]. In recent years, digital dermoscopy has revealed a new dimension of clinical morphology in pigmented skin tumors, becoming one of the most cost-effective non-invasive technique for early detection of skin cancer [3]. In dermoscopy, the diagnosis of skin tumors is frequently performed according to the *ABCD* rule (*A*: asymmetry, *B*: border irregularity,

C: color variegation and D: diameter) [4]. In order to facilitate early detection, numerous computerized methods have been developed [5]. In all these methods, skin tumor border segmentation [6] is a key step.

These methods are mainly based on thresholding, clustering and region growing [6-8]. These algorithms perform well for single tumors with clear borders. In all these techniques, they used color information in the non-uniform YC_bC_r and HSV color spaces. In the literature, several algorithms based on active contour (AC) models have also been proposed to segment single tumor or multi-tumor regions [9-11]. In these methods, the curve is defined by partial differential equations ($PDEs$). The $PDEs$ are controlled by an objective function. These active contour models are semi-automatic because of the selection of regularization parameters. The effectiveness of $DGVF$ [9] and $NBGP$ [10] methods degrades in the case of specular reflection or insufficient contrast, overlapping contours. In addition, contour re-initialization and the selection of regularization parameters are difficult. In [11], a region-based method was used based on a region-based active contour (RAC) model [12] to address the problems associated with $DGVF$ and $NBGP$.

On the other hand, in the literature about skin tumors-like region segmentation, the researchers have mainly considered a single level set (LS) initialization method to segment multiple regions. However, single initialization has several drawbacks: (1) computational inefficiency, (2) no guarantee of convergence and (3) difficult to get region-of-interest (ROI) objects. Overlapping of contours is also an issue that needs to be addressed in multi-region segmentation. Moreover, contrast enhancement has not been considered as a preprocessing step in the literature. Color information is often discarded. Nevertheless, there are a few approaches that use color information, albeit in non-uniform color spaces, mainly RGB or HSV.

To overcome these limitations, an improved perceptually-oriented region-based active contour (IRAC) method with effective image enhancement techniques is presented. In this $IRAC$ segmentation approach, a $CIECAM02$ color appearance model based uniform color space JCh is employed for the detection of the tumor region borders. Also, the homomorphic filter (HF) is utilized to reduce the specular reflection and a contrast improvement technique is applied to facilitate the segmentation process. In order to reduce the influence of hairs on segmentation, hair detection and exemplar-based inpainting techniques are utilized. With the proposed $IRAC$ model provides a guarantee of convergence, computational efficiency, while avoiding overlapping contours by means of a blob detection method. In fact, these blobs are used to initialize multiple level set curves instead of single contour initialization adopted by previous studies. Finally, to obtain smooth and refined tumor regions, in contrast to conventional RAC algorithms that manually select radius and lambda, the proposed $IRAC$ method automatically determines these parameters.

The remainder of this paper is organized as follows. Section 2 describes the color space transform step, which converts RGB image to $CIECAM02$ color appearance model. In section 3, the preprocessing step that enhances the dermoscopy images is described in detail. Multi-region segmentation model is then applied to tumor segmentation in Section 4. In Section 5, we present the experimental results. Finally, conclusions are given in Section 6.

2. **Color Space Transformation.** This new segmentation algorithm is intended to make the early diagnosis of skin cancer easier for the dermatologists. Accordingly, the algorithm has to emulate the perception of the medical expert in order to isolate from the image only the area of unhealthy skin. Therefore, the chosen color space must be a uniform. When dealing with almost uniform color spaces, $CIEL^*a^*b^*$ is the most widely used, especially when combined with the advanced distance metrics $CIE94$ and $CIEDE2000$.

This color system, accounts for chromatic adaptation when the illuminant of the scene is near day-light, the background is medium gray and the surround levels of luminance are moderate. However, it does not account for changes in background or luminance, can not predict brightness and colorfulness and give erroneous results when the illuminant of the scene is largely different from day-light.

The illumination changes the contrast of the scene, making some borders to disappear, especially in dark areas of the image [13]. Therefore, it is necessary to predict the perceived appearance of the dark tumor in a bright surrounding. Moreover, as stated in the literature, among the existing color spaces with their corresponding color formula, it is preferable to select a color appearance based uniform color space which is capable of considering viewing conditions [14]. A color appearance model, CAM, provides us the scene [15] as we would actually see it. This color appearance model [15] defines six dimensions of color appearance: brightness Q, lightness J, colorfulness M, chroma C, saturation s and hue h. In this space, first tristimulus values for both the sample and white are transformed to spectrally-sharpened cone responses as follows:

$$\begin{bmatrix} R \\ G \\ B \end{bmatrix} = M_{CAT02} \begin{bmatrix} X \\ Y \\ Z \end{bmatrix} \tag{1}$$

where M_{CAT02} is defined as:

$$M_{CAT02} = \begin{bmatrix} 0.7328 & 0.4296 & -0.1624 \\ -0.7036 & 1.6975 & 0.0061 \\ 0.0030 & 0.0136 & 0.9834 \end{bmatrix} \text{ and } M_B^{-1} = \begin{bmatrix} 1.0961 & -0.2789 & 0.1827 \\ 0.4544 & 0.4735 & 0.0721 \\ -0.0096 & -0.0057 & 1.0153 \end{bmatrix} \tag{2}$$

For chromatic adaptation transform the one used is the von Kries as given in Equations (3) and (4). Additionally, a variable D is used to specify the degree of adaptation. D is set to 1.0 for complete adaptation or discounting the illuminant (as is typically the case for reflecting materials). D is set to 0.0 for no adaptation, whereas intermediate values correspond to different degrees of intermediate chromatic adaptation and can be computed as follows:

$$\begin{aligned} R_c &= [Y_W (D/R_W) + (1 - D)] R \\ G_c &= [Y_W (D/G_W) + (1 - D)] G \\ B_c &= [Y_W (D/B_W) + (1 - D)] B \end{aligned} \tag{3}$$

where R_w, G_w and B_w are the RGB values of the reference white.

$$D = F[1 - (1/3.6) \times \exp((-L_A - 42)/92)] \tag{4}$$

Before obtaining the appearance correlates, some factors must be calculated as shown in Equation (5), including the background induction factor, n, the background and chromatic brightness induction factors, N_{bb} and N_{cb}, luminance level adaptation factor F_L and the base exponential nonlinearity, z.

$$\begin{aligned} k &= 1/(5L_A + 1) \\ F_L &= 0.2k^4 (5L_A) + 0.1 (1 - k^4)^2 (5L_A)^{1/3} \\ n &= Y_b/Y_w \\ N_{bb} &= N_{cb} = 0.725 (1/n)^{0.2} \\ z &= 1.48 + n^{1/2} \end{aligned} \tag{5}$$

In the post-adaptation step, the sample and white values are transformed from the sharpened cone responses to the Hunt-Pointer-Estevez cone responses as follows:

$$\begin{bmatrix} R' \\ G' \\ B' \end{bmatrix} = M_H M_{CAT02}^{-1} \begin{bmatrix} R_C \\ B_C \\ R_C \end{bmatrix}; \quad M_H = \begin{bmatrix} 0.38971 & 0.68898 & -0.07868 \\ -0.22981 & 1.18340 & 0.004641 \\ 0.00 & 0.00 & 1.0 \end{bmatrix} \quad (6)$$

A non-linear response compression is then performed as follows:

$$\begin{aligned} R'_a &= \left(400 \left(F_L R'/100\right)^{0.42} / \left(\left(F_L R'/100\right)^{0.42} + 27.13\right)\right) + 0.1 \\ G'_a &= 400 \left(F_L G'/100\right)^{0.42} / \left(\left(F_L G'/100\right)^{0.42} + 27.13\right) + 0.1 \\ B'_a &= 400 \left(F_L B'/100\right)^{0.42} / \left(\left(F_L B'/100\right)^{0.42} + 27.13\right) + 0.1 \end{aligned} \quad (7)$$

Finally, opponent responses (red-green and yellow-blue) can be obtained by

$$\begin{aligned} A &= \left[2R'_a + G'_a + (1/20) B'_a - 0.305\right] N_{bb} \\ a &= R'_a - 12G'_a/11 + B'_a/11 \\ b &= (1/9) \left(R'_a + G'_a - 2B'_a\right) \end{aligned} \quad (8)$$

Hue angle, h, is calculated from a and b:

$$h = \tan^{-1} \left(b/a\right) \quad (9)$$

Lightness, J, is obtained from the achromatic signals of the stimulus, A, and white, A_w:

$$J = 100 \left(A/A_W\right)^{cz} \quad (10)$$

Brightness, Q, is calculated from J and A_w:

$$Q = (4/c) \left(J/100\right)^{0.5} \left(A_W + 4\right) F_L^{0.25} \quad (11)$$

Chroma, C, is obtained by:

$$\begin{aligned} e &= \frac{1}{4} \left[\cos \left(h(\pi/180) + 2\right) + 3.8\right] \\ t &= (50000/13) N_c N_{cb} e \left(a^2 + b^2\right)^{1/2} / \left(R'_a + G'_a + (21/20) B'_a\right) \\ C &= t^{0.9} \left(J/100\right)^{0.5} \left(1.64 - 0.29^n\right)^{0.73} \end{aligned} \quad (12)$$

Colorfulness, M, is calculated using:

$$M = C F_L^{0.25} \quad (13)$$

Finally, saturation, s, is computed using:

$$s = 100 \sqrt{M/Q} \quad (14)$$

CIECAM02 does not explicitly construct a color space [16,17]. However, CIECAM02 lightness, chroma, and hue correlates (J, C, h) can be used to build a color space by considering them as cylindrical coordinates in the same way as $CIEL^*a^*b^*$ color space with L^*, C_{ab}^* and h_{ab}. But we can use an advanced metric very similar to CIEDE2000 [18] in $CIEL^*a^*b^*$ to correct the remaining non-uniformity, which is given as follows:

$$\begin{aligned} \Delta E_{02-OPT} &= \left[\left(\Delta J/k_J S_J\right)^2 + \left(\Delta C/(k_C S_C)\right)^2 + \left(\Delta H/(k_H S_H)\right)^2\right]^{1/2} \\ S_J &= 0.5 + \left(\bar{J}/100\right)^2; \quad S_C = 1 + 0.02\bar{C}; \quad S_H = 1 + 0.01\bar{C} \\ k_J &= k_C = k_H = 1 \end{aligned} \quad (15)$$

The JCh uniform color space is the color system adopted by the proposed method because of its uniformity and adaptation to human perception. This color space could be used for various tasks including image enhancement, feature extraction [19], segmentation and digital watermarking [20].

3. **Preprocessing.** A preprocessing step is crucial to facilitate the segmentation process. For assessing the illumination correction problem, the proposed algorithm performs homomorphic filtering (*HF*) in both, spatial and frequency domains, by processing the J plane of the *JCh* color space followed by a contrast adjustment in this color space. There are numerous image enhancement techniques such as Shearlet transform [21], and minimum mean brightness error dynamic histogram equalization (*MMBEDHE*) [22]. However, *the HF* method is another nonlinear effective image enhancement technique due to processing in frequency domain. It is also computational efficient and easy to implement.

3.1. **Specular reflection adjustment.** HF [23] is a generalized technique for nonlinear image enhancement and correction in both *RGB* and grayscale images. It concurrently normalizes the brightness of a dermoscopic image. In this study, the *HF* technique is adapted to human perception by adopting *JCh* color space and choosing J component. The method is briefly described here, and the interested reader should refer to [11] for more detailed information.

Consider the J component denoted as $s_J(x, y)$, which can be divided as the product of intensity illumination $i(x, y)$ and spatial-distribution reflectance $r(x, y)$, i.e.,

$$s_J(x, y) = i(x, y) \times r(x, y) \tag{16}$$

For illumination reduction by Fourier transform, we must model an image in an additive manner rather than a multiplicative one. Therefore, a logarithmic transform is applied to the $s_J(x, y)$ image to separate the illumination and reflectance components. By performing 2-D Fast Fourier transform (*FFT*) on the logarithmic transformed image $S_J(x, y)$, a Butterworth high-pass filter can be applied to amplify high frequency information. Then, after calculating the inverse Fourier transform and exponentiating, an enhanced image is obtained. This enhanced J image is used to replace the original one in the *CIECAM02* model. The resulting corrected image with its three components (J_{enh}, C and h) is denoted by $I_{CAM}(x, y)$. The result of this step is illustrated in Figure 1. In this figure, final $I_{CAM}(x, y)$ is presented in Figure 1(e).

3.2. **Contrast enhancement.** As described in Section 3.1, illumination correction is very important to achieve an effective enhancement solution but it is not enough for contrast improvement. An optimal solution is proposed for contrast enhancement that is adapted to human perception. Note that the *CIECAM02* color appearance model provides a more reliable separation between luminance and chrominance information than other color models.

Firstly we use C and h components of $I_{CAM}(x, y)$ of *CIECAM02* image while keeping J component constant. This is due to the fact that J component represents the luminance of image that has been corrected as explained in Section 3.1.

Let $C_{CAM}(x, y)$ and $h_{CAM}(x, y)$ denote the two selected components from $I_{CAM}(x, y)$ in (x, y) coordinate space. In order to determine a reliable color distribution in the two components, we have selected a method based on the standard deviation of these images. In contrast, the deviation method considers the probability of each color in the space and fully describes the color distribution in image.

The estimate of standard deviations σ_c and σ_h within $C_{CAM}(x, y)$ and $h_{CAM}(x, y)$ vectors we apply Equations (17) and (18):

$$\sigma_c = \left((1/n - 1) \times \sum_{L,M} (C_{CAM}(x, y) - \bar{C}_{CAM}(x, y))^2 \right)^{1/2} \tag{17}$$

$$\sigma_h = \left((1/n - 1) \times \sum_{L,M} (h_{CAM}(x,y) - \bar{h}_{CAM}(x,y))^2 \right)^{1/2} \tag{18}$$

where, n, L and M represent the total number of pixels and the height and width of the image respectively. $\bar{C}_{CAM}(x,y)$ and $\bar{h}_{CAM}(x,y)$ are the mean of $C_{CAM}(x,y)$ and $h_{CAM}(x,y)$ vectors. Next, updated components of $C_{CAM}(x,y)$ and $h_{CAM}(x,y)$ vectors, denoted by $C'_{CAM}(x,y)$ and $h'_{CAM}(x,y)$ are obtained as follows:

$$C'_{CAM}(x,y) = C_{CAM}(x,y) + (\rho - \sigma_c) \times (I_C - C_{CAM}(x,y)) \tag{19}$$

$$h'_{CAM}(x,y) = h_{CAM}(x,y) + (\omega - \sigma_h) \times (h_C - h_{CAM}(x,y)) \tag{20}$$

where $\rho = 0.00136$ and $\omega = -0.7036$ are constants whose values were determined empirically. The constant parameters I_C and h_C were determined by calculating the minimum and maximum intensity variations of the C component of the *CIECAM02* color appearance model, respectively. The selection of C is due to the better visualization of the texture information in that plane. The estimated contrast of $I_{CAM}(x,y)$ is updated by $C'_{CAM}(x,y)$ and $h'_{CAM}(x,y)$ components. After this homogeneity adjustment, the final contrast enhanced image $N_{CAM}(x,y)$ is obtained by:

$$N_{CAM}(x,y) = (I_{CAM}(x,y)_{Jch} - (J_{CAM}(x,y)_{\min}) / (J_{CAM}(x,y)_{\max} - J_{CAM}(x,y)_{\min})) \tag{21}$$

where $J_{CAM}(x,y)_{\min}$ and $J_{CAM}(x,y)_{\max}$ represent the minimum and maximum intensity values on the J plane of the $I_{CAM}(x,y)$ image.
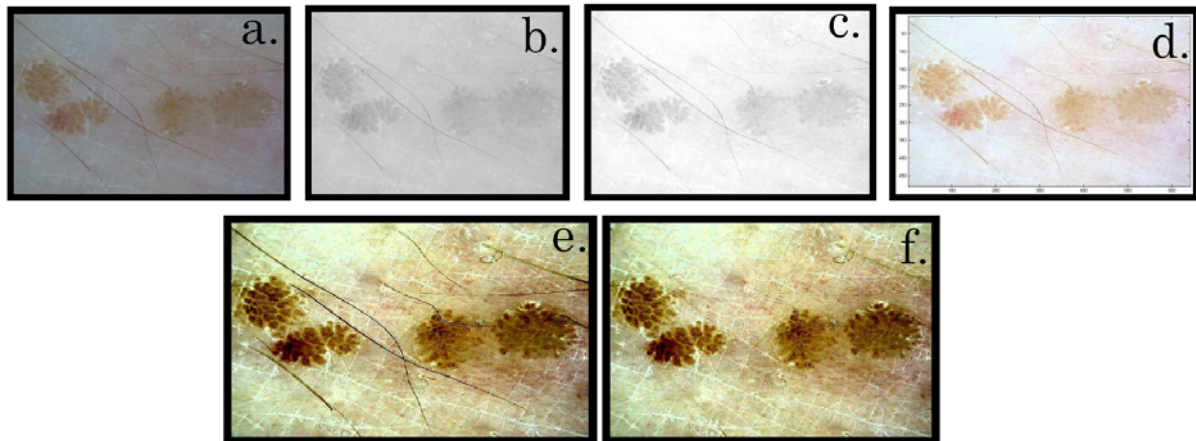

FIGURE 1. Illumination correction, contrast enhancement and hair removal: (a) original input image, (b) J component of the input image in the CIECAM02 color space, (c) illumination corrected image of the J component, (d) RGB illumination corrected image, (e) contrast enhancement output and hair removal result

3.3. **Hair removal.** Before performing segmentation, hairs in the tumor image must be removed without affecting the texture part of the tumor. In the literature, there are several techniques developed to remove hairs. However, many of them often leave behind undesirable blurring, disturb the texture of the tumor, and result in color bleeding. In the proposed algorithm we have employed the technique described in [11], but adapted to human perception thanks to the use of the *JCh* color space. The method first detects the lines in the image by using derivative of Gaussian, and then removes these lines using exemplar-based image inpainting technique. As illustrated in Figure 1(f), the hair pixels are effectively removed by this algorithm.

4. **Skin Tumor Segmentation Method.** Skin tumor images often contain multiple tumors. If a traditional algorithm tries to identify the edges of the tumors, it will most likely fail because the algorithm will look for a single contour to describe a group of pigmented tumors. Therefore, an effective multi-tumor segmentation algorithm is needed. In the present approach, we have used an improved version of the well known region-based active contour method using blob detection technique. However, the blob detection technique has the drawback of giving many false regions such as skin lines or regions inside the tumors. This method also requires an initial threshold value for rough segmentation. In this study, a minimum-error based thresholding procedure has been used [24] and circularity constraints have been imposed [25] to avoid these problems.

4.1. **Initial segmentation.** A threshold is determined automatically by using the minimum-error [24] technique applied to $N_{CAM}(x, y)$ image expressed in the approximately uniform JCh color space. This threshold value will be useful to obtain a rough segmentation of the tumor image. After that the blob detection technique is used. As it was already mentioned, the basic aim of this step is the initialization of multiple LS curves close to multi-region tumors. To select the largest circular blobs, the maximum area in pixels and estimated circularity descriptors are measured. In this manner, foreign objects such as skin lines or tiny dermoscopy gel artifacts are discarded. For quantifying circularity, we used the method developed by Haralick [25], which is based on mean and variance of radial distances. As the boundaries detected by this blob extraction method are not smooth, so a RAC technique is employed with the detected blobs initializing the LS curves.

4.2. **Segmentation refinement by IRAC model.** The RAC [11,12] model is used to segment multiple regions, simultaneously with some improvements. The advantage of this region-based technique when compared to edge-based methods is that it can segment multiple areas with "local energies" when "global energies" fail. In this study, the localization method employed is the Chan-Vese (CV) energy model for LS curves in the JCh color space. This CV approach for LS forms the snake curve through an energy minimization method, which has been widely used in several medical applications such as in brain MRI [26]. In the basic RAC model, Lankton and Tannenbaum [12] defined the energy function in terms of a generic force function as:

$$E(\phi) = \int\limits_{\Omega x} \delta\phi(x) \int\limits_{\Omega y} B(x, y).F(I(y), \phi(y)) dy dx \qquad (22)$$

where $E(\phi)$ represents the energy function for the level set ϕ, i.e. $C = \{\phi(x) = 0\}$. The generic force function F allows the curve to move freely. The Dirac delta function is denoted by $\delta\phi(x)$ while $B(x, y)$ function denotes local mask regions returning 1 when the point y is within a ball of radius r centered at x and 0 otherwise.

In this RAC method, the value of r is selected manually. By choosing r parameter, the smoothness condition inside and outside the contour is enforced. In the proposed $IRAC$ method, the value of r is determined by using the scale of the tumors region ($r = (Area(b))/100$). The smoothed version of Equation (22) is given by:

$$E(\phi) = \int\limits_{\Omega x} \delta(\phi(x)) \int\limits_{\Omega y} B(x, y).F(I(y), \phi(y)) \, dy dx$$
$$+ \lambda \int\limits_{\Omega x} \delta(\phi(x)) \left\| \nabla\phi(x) \right\| dx \qquad (23)$$

And the derivative of Equation (23) is calculated as:

$$\partial(\phi)/\partial t(x) = \delta(\phi(x)) \int\limits_{\Omega x} B(x,y).\nabla_{\phi(y)} F(I(y), \phi(y)) dy$$
$$+ \lambda \delta(\phi(x)) div(\nabla\phi(x)/|\nabla\phi(x)|) \tag{24}$$

where λ is a regularization term used for ensuring the smoothness of the curves. In previous RAC model, it must be defined and if fixed this could lead to an erroneous segmentation result. Moreover, each image would presumably have a different value of λ. In *IRAC*, to avoid this problem of local minima of the energy function $E(\phi)$, λ is determined automatically in a similar way to [12], i.e., by obtaining local interior and exterior points using Equations (28) and (29). Thus, to minimize the energy function $E(\phi)$ in terms of λ, a linear combination is defined as:

$$\lambda_v^u = \lambda u_x + (1 - \lambda) v_x \tag{25}$$

where $\lambda_v^u = (1 - \lambda)$ and $\lambda = (1 - \lambda_v^u)$ ensure that the segmentation solution can only operate on the boundaries. Next, the minimization Equation (25) is defined based on the mean interior (u_x) and exterior points (v_x) as:

$$\lambda_v^u = \left(\phi(x).\sum_{i=1}^{n} u_x^i\right) \Big/ \left(\sum_{i=1}^{n} u_i - 1 + \in\right) - \left(\sum_{i=1}^{n} v_x^i\right) \Big/ \left(\left(\sum_{i=1}^{n} v_i\right)^2 - 1 + \in\right) \tag{26}$$

Consequently, the algorithm calculates λ, the smoothing parameter, based on a level set $\phi(x)$ points of the energy function $E(\phi)$. In this segmentation model, the energy function is modeled by *CV* energy, which is defined as:

$$E_{CV}(\phi) = \int\limits_{\Omega y} H\phi(y)(I(y) - u)^2 + (1 - H\phi(y))(I(y) - v)^2 \, dy \tag{27}$$

where u and v are the local interior and exterior points, respectively and $H\phi(y)$ is the Heaviside function. The mean interior and exterior points of (u, v) denoted by (u_x, v_x) are calculated by the following equations:

$$u_x = \int\limits_{\Omega y} B(x,y).H\phi(y).I(y)dy \Big/ \int\limits_{\Omega y} B(x,y).H\phi(y)dy \tag{28}$$

$$v_x = \int\limits_{\Omega y} B(x,y).(1 - H\phi(y)).I(y)dy \Big/ \int\limits_{\Omega y} B(x,y).(1 - H\phi(y))dy \tag{29}$$

To improve efficiency, we have also computed values in a narrow band around the zero level set. For a detailed numerical implementation of this CV model, the interested reader is referred to [11,12]. Moreover, in order to avoid overlapping contours issue, we have integrated a conditional function derived from the initial blobs. For example, two LS curves merge in a single LS curve if there only one blob detected in that region. Similarly, if an LS curve is going to split into two LS curves if there are two blobs detected in that region. As a result, the CF condition saves the overlapping contour problem, which can be integrated in many AC-based segmentation techniques.

5. **Results.** The proposed multi-tumor segmentation method was tested on a set of 175 dermoscopic images. This dataset consists of 80 benign (B) and 190 malignant melanoma (MM) tumors. Specular reflection, low contrast, and hair artifacts were generally present in these images. Therefore, the algorithm begins enhancing the images using the proposed

preprocessing steps. In order to obtain a ground truth for each of the images in the dataset, we requested an experienced dermatologist to manually draw the tumor borders on each of the enhanced images. The results of the proposed $IRAC$ method were compared to three state-of-the-art active contour (AC) models: CV, Geodesic Active Contours (GAC) and traditional RAC. The experiments were performed on a 2.3 GHz dual-core 64-bit AMD processor with 4GB $DDR2$ RAM. The algorithms were implemented in MATLAB 7.6.0.324 ® (The Mathworks, Natick, MA).

An error measure was used to quantify the quality of segmentation:

$$ER_i = (A_i(GT) \oplus A_i(AS))/(A_i(GT) + A_i(AS)) \times 100 \tag{30}$$

where the area determined from the ground truth is denoted by $A_i(GT)$ and the area segmented by a computerized method is represented by $A_i(AS)$ for each of the outlines. The value of i depends upon number of tumors in an image (t_n). In order to calculate the total error, we used mean and standard deviation given by:

$$\mu = 1/t_n \sum_{i=1}^{t_n} ER_i \tag{31}$$

$$\sigma = \left(\left(\sum_{i=1}^{t_n} (ER_i - \mu)^2 \right) \bigg/ (t_n - 1) \right)^{1/2} \tag{32}$$

The $IRAC$ multi-tumor segmentation results from three sample images are given in Figure 2. The red contour is drawn manually from the ground truth, while the blue one is obtained from the $IRAC$ segmentation model. The proposed method obtains a significant improvement in mean and standard deviation error. In each figure of Figure 2, the error ($\mu \pm \sigma$) of the $IRAC$ method are 3.24 ± 1.23, 4.20 ± 2.10 and 1.24 ± 0.08 when compared with the ground truth, respectively. These results demonstrate that the $IRAC$ model is an effective segmentation method that mimics human visual perception.

In order to compare the $IRAC$ segmentation method with other multi-region segmentation algorithms, some parameter values should be defined. Elasticity, rigidity, viscosity, regularization, and time step parameters were set as $\alpha = 0.5$, $\beta = 0.1$, $\gamma = 1.0$ and $\lambda = 1.5$ and $t = 0.1$ respectively. After converting the RGB image to a luminance image, a minimum-error thresholding method was performed for the initialization of the single contour methods. For multi LS curve initialization method, the blob detection method was performed on the J component of the JCh color space. The number of iterations for multi LS curve initialization was set to 160, while the same parameter was set to 350 in the single contour approach.

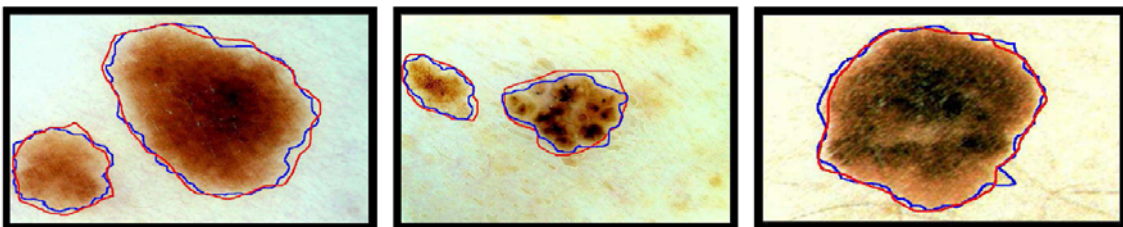

FIGURE 2. Multi-tumor segmentation results, where contours detected by IRAC (blue outline), manual segmentation by expert (red outline)

The comparison of $IRAC$ with CV, GAC and RAC models are shown in Figure 3 on an acral melanoma. In this type of tumor, the border is highly irregular and fuzzy and therefore very difficult to determine. However, the $IRAC$ segmentation model effectively
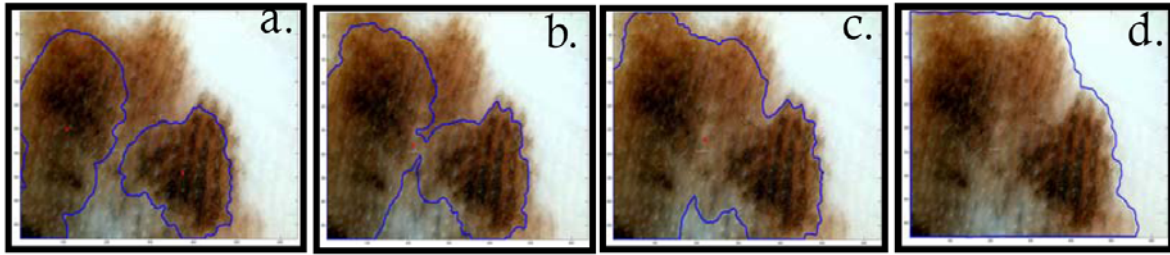
FIGURE 3. Comparison of segmentation results after illumination correction, and contrast enhancement in case of acral melanomas by (a) CV (b) GAC (c) RAC, (d) IRAC models

TABLE 1. Segmentation performance comparisons in terms of error and CPU time

Methods	Single contour initialization		Multi-contour initialization	
	$T_1(s)$	$\mu \pm \sigma$	$T_2(s)$	$\mu \pm \sigma$
CV	46.10	41±07.80	32.72	8.86±4.79
GAC	39.26	12.20±06.06	25.19	7.23±3.56
RAC	17.45	9.21±04.93	12.10	6.40±3.15
IRAC	17.89	8.38±04.10	12.63	4.10±2.42

separates the tumor area from the healthy skin. Computational cost is an important factor that determines the practical applicability of a segmentation algorithm. Mean and standard deviation errors and execution times for the four segmentation methods in terms of single contour, and multi-contour initialization are summarized in Table 1. This table demonstrates the advantage of multiple LS curves initialization technique, which has not been addressed in the past to segment multiple objects. The IRAC method is significantly faster when compared with CV and GAC, but similar to RAC in both cases. Despite the fact that we have added extra steps to calculate the regularization parameters and impose conditional function, the computational requirements of IRAC is approximately equal to those of RAC. Consequently, we can conclude that IRAC converges faster due to the better selection of the lambda parameter.

6. **Conclusions.** In this paper, a novel approach for skin tumor segmentation has been presented. The algorithm is designed to match human perception due to the use of the approximately uniform color space *JCh* based on the *CIECAM02* color appearance model. The proposed segmentation method was tested on a set of 175 dermoscopic skin cancer images consist of benign: 80 and malignant melanoma: 190 tumors. The experiments, based on the ground truth contributed by an expert physician, indicate that our method provides an effective solution for the segmentation of fuzzy multi-tumor in dermoscopy images. Although the method has been tested on skin tumor images, it could be applied to any kind of image that contains blob-like regions, because it is not application-specific. In the future work, surrounding condition of the images will be investigated to determine the best parameters for the *CIECAM02* color model. We will also compare the obtained results with the ones given with the same technique in *CIEL***a***b** approximately uniform color space.

REFERENCES

[1] D. S. Rigel, Malignant melanoma: Perspectives on incidence and its effects on awareness, diagnosis, and treatment, *CA Cancer J. Clin.*, vol.46, no.4, pp.195-198, 1996.

[2] A. Jemal, R. Siegel, J. Xu and E. Ward, Cancer statistics, *CA Cancer J. Clin.*, vol.60, pp.277-300, 2010.

[3] G. Argenziano, H. P. Soyer, S. Chimenti, R. Talamini, R. Corona, F. Sera et al., Dermoscopy of pigmented skin lesions: Results of a consensus meeting via the Internet, *J. Am. Acad. Dermatol.*, vol.48, no.5, pp.679-693, 2003.

[4] F. Nachbar, W. Stolz, T. Merkle, A. B. Cognetta, T. Vogt et al., The ABCD rule of dermatoscopy: High prospective value in the diagnosis of doubtful melanocytic skin lesions, *J. Amer. Acad. Dermatol.*, vol.30, no.4, pp.551-559, 1994.

[5] M. E. Celebi, H. A. Kingravi, B. Uddin et al., A methodological approach to the classification of dermoscopy images, *Comput. Med. Imag. Grap.*, vol.31, no.6, pp.362-373, 2007.

[6] M. E. Celebi, H. Iyatomi, G. Schaefer and W. V. Stoecker, Lesion border detection in dermoscopy images, *Comput. Imag. Grap.*, vol.33, no.3, pp.148-153, 2009.

[7] H. Iyatomi, H. Oka, M. E. Celebi et al., An improved Internet-based melanoma screening system with Dermatologist-like tumor area extraction algorithm, *Comput. Med. Imag. Grap.*, vol.32, no.7, pp.566-579, 2008.

[8] D. D. Gomez, C. Butakoff, B. K. Ersboll and W. V. Stoecker, Independent histogram pursuit for segmentation of skin lesions, *IEEE T Biomed. Eng.*, vol.55, no.1, pp.157-161, 2008.

[9] J. Tang, A multi-direction GVF snake for the segmentation of skin cancer images, *Pattern Recogn.*, vol.42, no.6, pp.1172-1179, 2009.

[10] X. Yuan, N. Situ and G. Zouridakis, A narrow band graph partitioning method for skin lesion segmentation, *Pattern Recogn.*, vol.42, no.6, pp.1017-1028, 2009.

[11] Q. Abbas, I. Fondón and M. Rashid, Unsupervised skin lesions border detection via two-dimensional image analysis, *Comput. Meth. Prog. Bio.*, 2010.

[12] S. Lankton and A. Tannenbaum, Localizing region-based active contours, *IEEE T Image Process*, vol.17, no.11, pp.2029-2039, 2008.

[13] E. F. Kelley, M. Lindfors and J. Penczek, Display daylight ambient contrast measurement methods and daylight readability, *J. Society of Information Display*, vol.14, no.11, pp.1019-1030, 2006.

[14] D. H. Alman, R. S. Berns, G. D. Snyder and W. A. Larsen, Performance testing of color-difference metrics using a color tolerance dataset, *Color Research & Application*, vol.14, no.3, pp.139-151, 1989.

[15] N. Moroney, M. Fairchild, R. Hunt, C. Li, M. Luo and T. Newman, The CIECAM02 color appearance model, *Proc. of IS & T/SID 10th Color Imaging*, pp.23-27, 2002.

[16] C. J. Li and M. R. Luo, Testing the robustness of CIECAM02, *Color Research & Application*, vol.30, no.2, pp.99-106, 2005.

[17] M. D. Fairchild, A revision of CIECAM97s for practical applications, *Color Research & Applications*, vol.26, no.6, pp.418-427, 2001.

[18] P. Urban, R. S. Berns and M. R. Rosen, Constructing euclidean color spaces based on color difference formulas, *Proc. of IS&T/SID 15th Color Imaging Conference: Color Science and Engineering Systems, Technologies, and Applications*, pp.77-82, 2007.

[19] Y.-Q. Lei, K.-Y. Chau, Z.-M. Lu and W.-H. Ip, DCT-domain global feature and DWT-domain least-squares line fitting based local feature for robust image hashing, *International Journal of Innovative Computing, Information and Control*, vol.6, no.6, pp.2513-2522, 2010.

[20] D. Xiao and F. Y. Shih, A reversible image authentication scheme based on chaotic fragile watermark, *International Journal of Innovative Computing, Information and Control*, vol.6, no.10, pp.4731-4742, 2010.

[21] J. Pan, C. Zhang and Q. Guo, Image enhancement based on the shearlet transform, *ICIC Express Letters*, vol.3, no.3(B), pp.621-626, 2009.

[22] F. Hossain and M. R. Alsharif, Minimum mean brightness error dynamic histogram equalization for brightness preserving image contrast enhancement, *International Journal of Innovative Computing, Information and Control*, vol.5, no.10(A), pp.3249-3260, 2009.

[23] M. J. Seow and V. K. Asari, Ratio rule and homomorphic filter for enhancement of digital colour image, *Neurocomputing*, vol.69, pp.954-958, 2006.

[24] J. Kittler and J. Illingworth, Minimum error thresholding, *Pattern Recogn.*, vol.19, pp.41-47, 1986.

[25] R. M. Haralick, A measure for circularity of digital figures, *IEEE T Syst. Man Cybern.*, vol.SMC-4, pp.394-396, 1974.

[26] Z. Chen, T. Qiu and S. Ruan, A segmentation algorithm for brain MR images using fuzzy model and level sets, *International Journal of Innovative Computing, Information and Control*, vol.6, no.12, pp.5565-5574, 2010.